nature physics

ARTICLES

PUBLISHED ONLINE: 9 FEBRUARY 2014 | DOI: 10.1038/NPHYS2870

Visualization of electron nematicity and unidirectional antiferroic fluctuations at high temperatures in NaFeAs

E. P. Rosenthal[1], E. F. Andrade[1], C. J. Arguello[1], R. M. Fernandes[2], L. Y. Xing[3], X. C. Wang[3], C. Q. Jin[3], A. J. Millis[1] and A. N. Pasupathy[1]*

Superconductivity in the iron pnictides is often closely connected to a nematic state in which the tetragonal symmetry of the crystal is spontaneously broken. Determining the dominant interactions responsible for this symmetry breaking is essential to understanding the superconducting state. Here, we use atomic-resolution variable-temperature scanning tunnelling spectroscopy to probe the nanoscale electronic structure of the nematically ordered, parent pnictide NaFeAs and compare it with non-nematic LiFeAs. Local electronic nematicity is only manifest in NaFeAs and is found to persist to high temperatures in the nominally tetragonal phase of the crystal. The spatial distribution and energy dependence of the electronic anisotropy at high temperatures is explained by the persistence of large-amplitude, short-range, unidirectional, antiferroic fluctuations, indicating that strong density-wave fluctuations exist and couple to near-Fermi surface electrons even far from the structural and density-wave phase boundaries.

The nature of the normal state from which superconductivity emerges in unconventional superconductors remains a mystery. It is suspected that electronic interactions present in the normal state play a key role in the formation of the superconducting state[1]. In both the cuprate and the pnictide phase diagrams magnetically ordered states exist in proximity to the superconducting state, with the pnictides furthermore exhibiting orbital ordering[2,3]. A crucial further feature of the pnictides is the appearance of a 'nematic' phase in which the tetragonal rotational symmetry of the ideal pnictide lattice is spontaneously broken below a temperature T_S. In the nematic state, the tetrahedral bonding environment of the iron arsenide plane is distorted to an orthorhombic phase in which the nearest neighbour iron–iron distances in the *a* and *b* directions become inequivalent[4], and the occupation degeneracy of the $3d_{xz}$ and $3d_{yz}$ iron orbitals is lifted[5]. In mathematical terms, the symmetry is lowered from C_4 (symmetry of the square) to C_2 (symmetry only under 180° rotation). At a temperature $T_{SDW} \leq T_S$, magnetic order sets in with a wave vector $Q_a = ((\pi/a_0), 0)$, where a_0 is the longer iron–iron distance in the orthorhombic phase[6]. The structural (nematic) and magnetic (stripe) transitions seem to be intimately linked, as T_{SDW} and T_S track each other across the phase diagram, even inside the superconducting dome[7,8]. Recent bulk transport and scattering measurements have suggested that the nematic phase is driven by electronic, rather than lattice, degrees of freedom[5,9–13] and is observed in all electronic channels—charge[13–15], orbital[5] and spin[11,16]. Spin order and spin fluctuations[17–21] (which couple quadratically to nematicity) as well as orbital order[22,23] and orbital fluctuations[24] (which can couple linearly) have been invoked to explain the nematicity. However, the dominant interaction responsible for the nematic ordering and fluctuations remains unknown and identifying it is a key experimental goal.

Scanning tunnelling microscopy (STM) studies have successfully visualized local, anisotropic electronic states in the low-temperature orthorhombic state of pnictides[25–27]. However, because they are performed at low temperatures, these measurements are sensitive only to the coupling between nematicity and the saturated order parameter values and do not provide information about fluctuations. In this paper, we use variable temperature scanning tunnelling spectroscopy (STS) with atomic scale spatial sensitivity and millivolt energy resolution to image the electronic wavefunctions of NaFeAs at temperatures both below and above the magnetic and structural phase boundaries and thus gain new insights into the physics of the ordered electronic nematic state and the high-temperature state that gives rise to it. We choose to investigate the 111 family of iron arsenides AFeAs, with A being an alkali metal, because it has been shown that cleaving the crystals produces nonpolar surfaces[28–32]. NaFeAs has a structural transition at $T_S = 52$ K and a magnetic transition at $T_{SDW} = 41$ K. The unusually large temperature separation between these transitions allows us to sensitively probe the electronic structure in all three phases of the material. LiFeAs is chosen as a reference material because it has neither a structural nor a magnetic transition down to low temperature[33–35]. Both NaFeAs and LiFeAs have a low-T superconducting state, but our measurements are taken above this transition temperature. An STM topographic image typical of both of these materials (in this case LiFeAs) is shown in Fig. 1a. A square lattice of alkali atoms is observed, which is consistent with previous measurements for both materials[28–32]. The iron atoms (shown schematically in the lower left portion of the figure) lie below the alkali atoms, with in-plane position approximately half-way between pairs of Li atoms. Differences in the position of the out-of-plane As atoms (not shown) make the two Fe sites

---

[1]Department of Physics, Columbia University, New York, New York 10027, USA, [2]School of Physics and Astronomy, University of Minnesota, Minneapolis, Minnesota 55455, USA, [3]Beijing National Laboratory for Condensed Matter Physics, Institute of Physics, Chinese Academy of Sciences, Beijing 100190, China. *e-mail: apn2108@columbia.edu

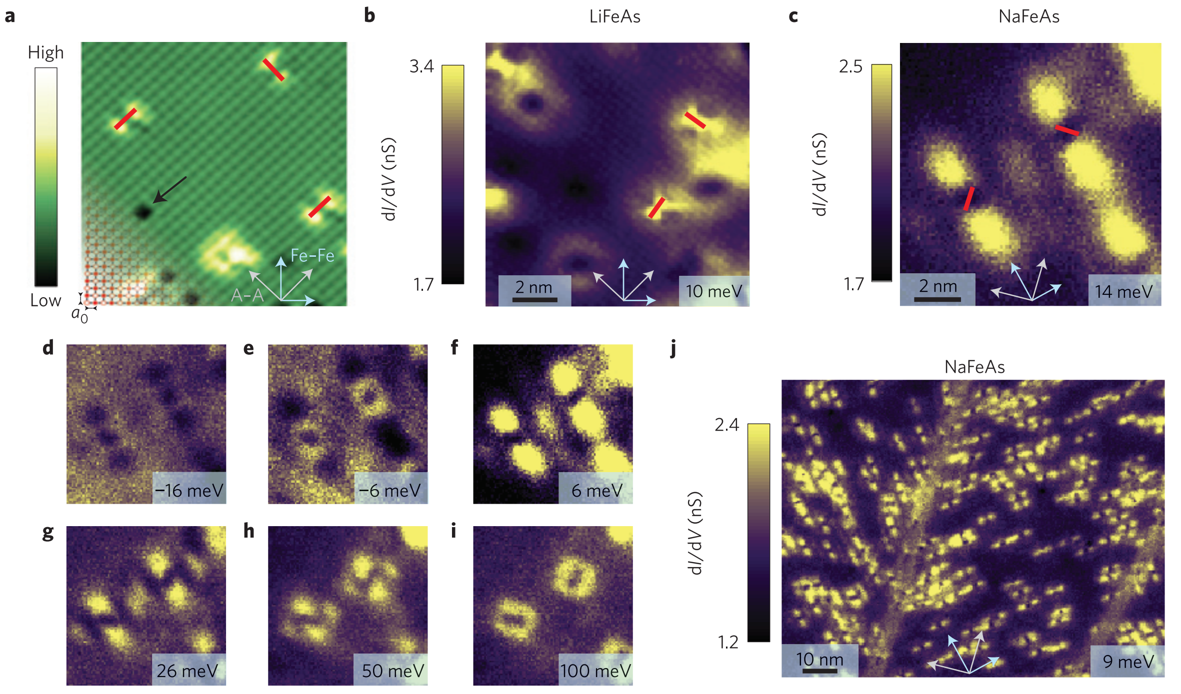

Figure 1 | Topographic STM and STS maps of LiFeAs and NaFeAs at low temperatures. **a**, Constant-current STM topograph of LiFeAs ($V=-120$ mV, $I=270$ pA, $T=39$ K). The alkali atoms are observed on the surface layer, and the underlying iron atoms are illustrated at the lower left side. The two inequivalent positions of the iron atoms are shown with filled and unfilled circles. An alkali vacancy is identified with a black arrow, and red lines indicate the size and orientation of iron site defects. Grey arrows identify the alkali–alkali directions, and cyan arrows identify the orientation of the Fe–Fe lattice (continued for the rest of Fig. 1). **b**, Differential conductance (dI/dV) map ($V=-120$ mV, $I=270$ pA, $T=39$ K) of LiFeAs. The iron defects have prominent signatures in the dI/dV maps with the same size and symmetry as the topographic features, as indicated by the red lines. **c**, dI/dV map of NaFeAs ($V=-100$ mV, $I=300$ pA, $T=26$ K) showing prominent features that are oriented along one Fe–Fe direction at 45° to the crystallographic axes. The size and orientation of iron site defect that produce the features are indicated by red lines. **d**–**i**, dI/dV maps at different energies of the area shown in **c**, showing a clear variation in the contrast and size of the features as a function of energy. **j**, Large-area dI/dV image of NaFeAs (same junction conditions and temperature as **d**) showing the universality of the spectroscopic features and the presence of domains where the unidirectional features rotate by 90°.

inequivalent (indicated by filled and unfilled circles). Large-area topographs in both materials reveal the presence of several types of crystalline defects, which is typical of all samples studied[28,31,32]. The STM topographic features produced by some of these defects (such as the alkali vacancy, black arrow, Fig. 1a) do not break the local C_4 symmetry, whereas other defects (such as the iron site defects[32] which are visualized as the bright, yellow, 'dumbbell'-shaped features in Fig. 1a) do reduce the local symmetry to C_2 in their immediate vicinity. These iron defects produce topographic features whose symmetry axes are along the alkali–alkali (A–A) nearest neighbour directions[32] and whose orientation is determined by the iron position underneath the midpoint of the A–A bond.

As expected, all defects modify the local density of states (LDOS) in their immediate vicinity. However, the nature of the changes in the LDOS is very different in LiFeAs and NaFeAs. We illustrate this by showing STS images at energies of $E=10$ meV and $E=14$ meV around two inequivalent iron-site defects in LiFeAs (Fig. 1b) and NaFeAs (Fig. 1c), respectively. We can see C_2 symmetric features in both cases. Figure 1b, which has been obtained on LiFeAs at 39 K, contains two inequivalent C_2 symmetric features that arise from two inequivalent iron defects (see Supplementary Fig. 1 for the corresponding topographic image). The spectroscopic signatures of the defects have roughly the same size (about 10 Å) and point in the same directions (Li–Li) as the corresponding topographic features, whose sizes and orientations are indicated by red lines. We find that in LiFeAs there are an equal number of iron defects on average in each of the two inequivalent positions, resulting in an equal number of features oriented along either Li–Li axis. Thus, although the electronic structure of LiFeAs is not C_4 symmetric at the atomic scale as a result of iron site defects, averages over larger length scales of the electronic structure cancel out these differences from the local defect states and become C_4 symmetric. Figure 1c shows a spectroscopic image of NaFeAs measured at 26 K, deep within the SDW phase. As in Fig. 1b, we identify the topographic size and orientation of two inequivalent iron defects with red lines. Unlike in LiFeAs, the spectroscopic signatures of the defects point along the same direction, 45° with respect to the Na–Na axes, corresponding to the Fe–Fe nearest neighbour direction. These spectroscopic features also have a much greater spatial extent (typically 50 Å) than the topographic signatures of the defects. Consequently, C_4 symmetry is broken over large scales compared with the defect separation. The spatial extent and anisotropy of the features obtained on NaFeAs have a pronounced energy dependence, as seen in Fig. 1d–i, whereas the energy dependence in the case of LiFeAs is much weaker (see Supplementary Fig. 1).

A second key difference between LiFeAs and NaFeAs is the relationship between the nature of the defect and the changes in the LDOS in the spectroscopic images. In the case of LiFeAs, different defects produce different patterns, and in particular the defects that do not break C_4 symmetry in topography do not do so in spectroscopy either (see Supplementary Information). On the other hand, in NaFeAs, the spectroscopic features seen in large-area maps are completely independent of the nature of the defect, as shown by the spectroscopic survey over a much larger area in Fig. 1j (see also Supplementary Fig. 3). This field of view contains many types of defects that all produce the same spectroscopic feature and clearly depicts the presence of two domains corresponding to the two inequivalent ways of breaking C_4 symmetry. The typical size of

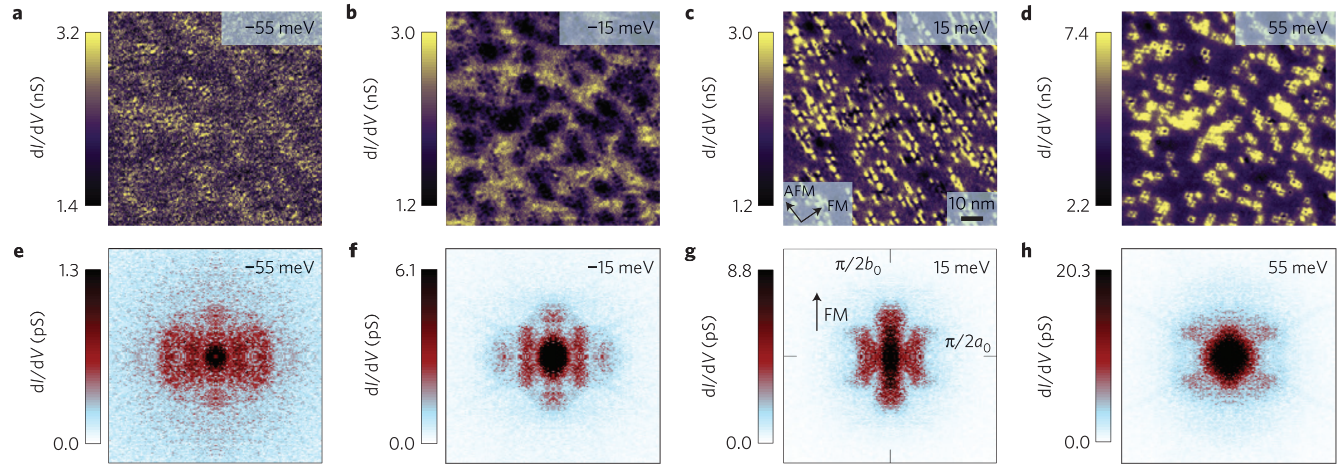

Figure 2 | STS maps of NaFeAs in real and Fourier space in the SDW phase. a–d, Large-area differential conductance maps on NaFeAs ($V = -100$ mV, $I = 300$ pA, $T = 26$ K). Arrows in **c** indicate ferromagnetic (FM) and antiferromagnetic (AFM) directions. **e–h**, Corresponding FFT images. The FFT images show well-defined structures whose wavelengths and intensities are energy dependent. The size of the images is half of the single Fe unit cell Brillouin zone.

domains observed at low temperature is 1–2 μm in our samples, which is consistent with the size of twin domains in pnictides[36].

Similar anisotropic, LDOS features have been observed by STM in the SDW phase of other iron-based superconductors such as $Ca(Fe_{1-x}Co_x)_2As_2$ (refs 26,37) and FeSe (ref. 25). In the case of $Ca(Fe_{1-x}Co_x)_2As_2$, the anisotropic features seen were weakly dependent on energy and were attributed to the modification of the local electronic structure by Co defects. In our case, the anisotropic features observed are independent of defect type, and their shape and intensity exhibit a strong energy dependence; these spectroscopic properties are indicative of quasiparticle interference (QPI) arising from the anisotropic electronic structure in the SDW phase[38]. In QPI, defects serve as scattering centres and produce interference patterns that change in contrast and wavelength as a function of energy[39]. Accordingly, we examine the two-dimensional Fast Fourier transform (FFT) of conductance images to understand the momenta of quasiparticles involved in the scattering processes[26]. To achieve high Fourier space resolution, we obtained spectroscopic images over a large, 110 nm square field of view. These real space images are shown for select energies in Fig. 2a–d, which demonstrate that the unidirectional features persist over a range of energies around the Fermi energy. The FFTs of the real space images are shown in Fig. 2e–h (FFT procedure described in Supplementary Information). The rich structure seen in the FFTs is strongly energy dependent, as expected from QPI, and we do not see evidence of the static scattering wave vectors that have been observed in $Ca(Fe_{1-x}Co_x)_2As_2$ (refs 26,37).

Having seen unidirectional structure in the STS images at low temperature, we ask how the STS images evolve as one raises the temperature beyond T_{SDW} (41 K) and T_S (52 K). We have performed STS measurements on a series of samples at many temperatures between 20 and 85 K. Figure 3 plots the raw STS data through both phase transitions at temperatures of 26, 38, 46, 54, 61, and 75 K along with their respective FFT images. All images are plotted at an energy of $E = 10$ meV and are obtained under similar junction conditions. We can clearly see that the unidirectional features which are seen below T_{SDW} persist at temperatures far above the structural transition, showing C_4 symmetry breaking by low-energy electronic states over the STM field of view. The C_4 symmetry breaking gets weaker with increasing temperature and is not experimentally measurable at temperatures above ∼90 K.

A potential cause for concern in interpreting STM data on any bulk crystal is the relationship between bulk and surface electronic structure. We have two pieces of evidence that data obtained from surface probes such as STS are representative of bulk behaviour. First, a clear SDW gap is observed in the spectrum (see ref. 28 and also the discussion below) that disappears near the bulk SDW transition of 41 K. Second, angle-resolved photoemission spectroscopy (ARPES, also a surface probe which averages over a wide area) data from similar crystals[40,41] indicates that the temperature dependent band structure of NaFeAs at the surface is truly representative of the bulk crystal properties. In particular, the orthorhombic to tetragonal transition is clearly observed in ARPES from the temperature dependence of the bands.

We now consider the implications of our results for the physics of the pnictide materials. The first point, independent of any theoretical analysis, is the observed persistence of local C_4 symmetry breaking in the local electronic structure to temperatures ∼90 K, well above the measured structural phase transition temperature $T_S = 52$ K. We believe this is a consequence of the combination of a small, external strain (Methods) and the rapidly growing nematic susceptibility inferred from electrical resistivity measurements on detwinned crystals[12,42] . As we now show, the STM data reveals further important physics beyond the C_4 symmetry breaking, namely that strong, short-range, antiferroic fluctuations play a key role in the electronic structure, even at temperatures up to 90 K, well into the paramagnetic nominally symmetry-unbroken phase.

The key features in the FFT images that we seek to understand are shown in Fig. 4a–c, taken at the Fermi energy at temperatures of 26 K, 46 K and 61 K respectively. At all three temperatures there is a strong signal along rods centred at $Q_x = 0$ and $Q_x = q_D \equiv \pm 0.15(\pi/a_0)$. The breaking of rotational symmetry is evident in the alignment of the rods (in this image, parallel to the y direction). It will be shown that the structures at $Q_x = \pm q_D$ are accounted for by antiferroic fluctuations.

To analyse the FFT images more quantitatively, we turn to the theory of QPI, which states[43] that the observed spatial modulations in dI/dV at energy ω are directly proportional to impurity-induced modulations of the local electronic density of states $\delta N(R, \omega)$. The Fourier transform may be computed from the electron Green's function $G(\mathbf{k}, \omega)$, which describes propagation of an electron of energy ω and crystal momentum $\mathbf{k}$ in a defect-free material, and the T-matrix $T_{\mathbf{r}_{imp}}(\mathbf{k}, \mathbf{k}+\mathbf{Q}; \omega)$, which describes the total scattering amplitude of an electron from crystal momentum $\mathbf{k}$ to crystal momentum $\mathbf{k}+\mathbf{Q}$ by a defect at position $\mathbf{r}_{imp}$

$$\delta n(\mathbf{Q}, \omega) = \mathrm{Im} \int \mathrm{d}\mathbf{k} G(\mathbf{k}, \omega) T_{\mathbf{r}_{imp}}(\mathbf{k}, \mathbf{k}+\mathbf{Q}; \omega) G(\mathbf{k}+\mathbf{Q}, \omega) \qquad (1)$$

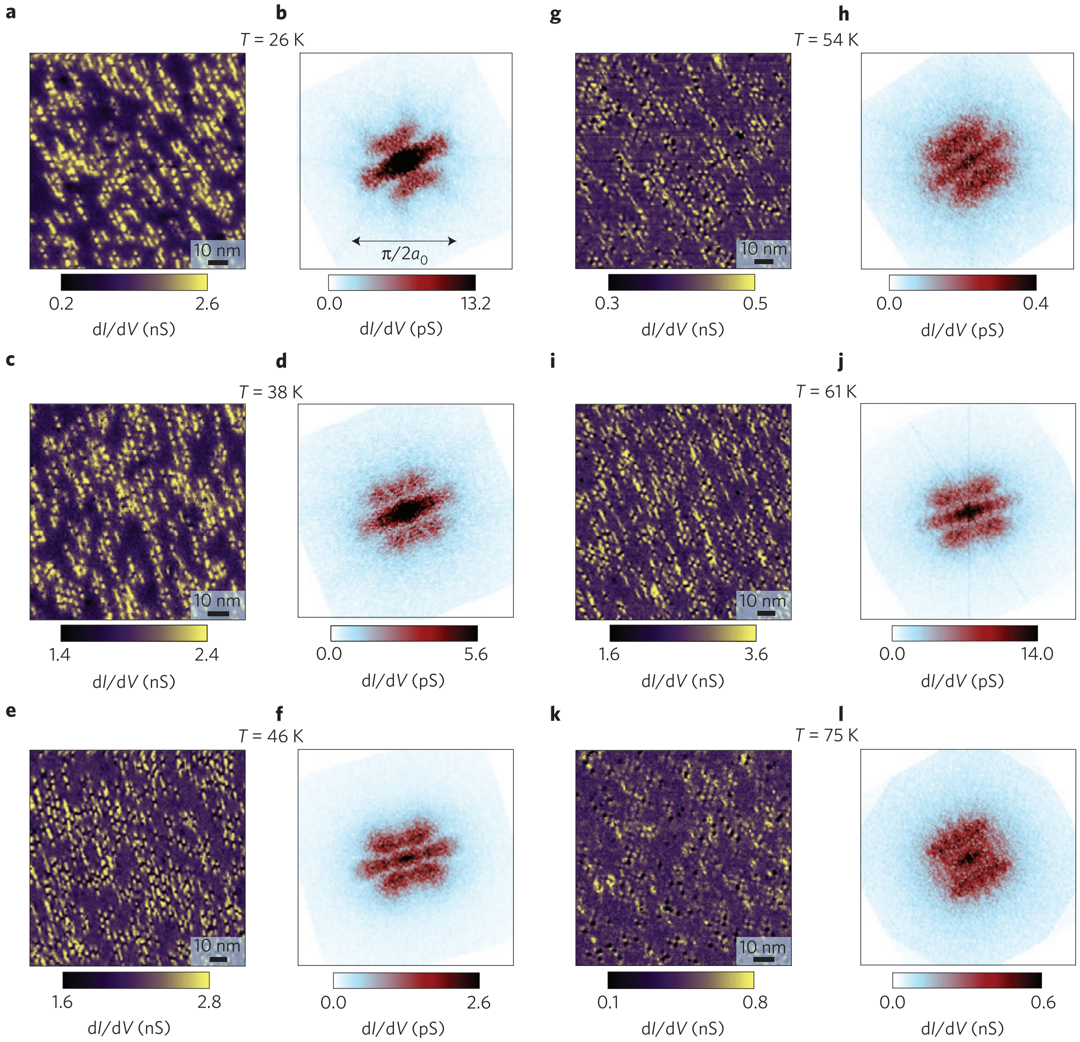

Figure 3 | Temperature dependence of anisotropic STS features in real and Fourier space. **a**,**c**,**e**,**g**,**i**,**k**, Large-area maps of the differential conductance at 10 meV at different temperatures on NaFeAs. The raw images show that the unidirectional features persist up to the highest temperatures shown. However, the intensity of the unidirectional features decreases with increasing temperature and becomes weak above 80 K. **b**,**d**,**f**,**h**,**j**,**l**, The corresponding FFT images (same scale as Fig. 2e–h). Junction settings for 26, 38, 46 and 61 K are $V = -100$ mV and $I = 300$ pA. Junction settings for 54 and 75 K are $V = -50$ mV and $I = 300$ pA. It is seen that the same basic structure exists in all the FFT images, even above $T_{\mathrm{SDW}} = 41$ K and $T_{\mathrm{S}} = 52$ K. Images in **a**–**d** and **e**–**l** are from different samples.

The signal at a given wavevector **Q** in the QPI can therefore arise either from the Green's function (bandstructure) of the material or from structure in the T-matrix.

We first consider the effect of the experimentally determined NaFeAs bandstructure on QPI. For the case of the structureless T-matrix, the structure in the QPI pattern is found to be well captured by the joint density of states (JDOS) $\int \mathrm{d}\mathbf{k}\,\mathrm{Im}[G(\mathbf{k},\omega)]\mathrm{Im}[G(\mathbf{k}+\mathbf{Q},\omega)]$ (ref. 44). The band structure of high-temperature tetragonal NaFeAs observed in ARPES at low energies (<200 meV; refs 40,41) consists of nearly circular hole pockets at the Γ point and elliptical electron pockets at the X and Y points of the unfolded single Fe unit cell (see Supplementary Fig. 5). At low temperatures, long-range nematic and SDW order sets in. As a result, the zone-centre circular pockets become elliptical, the two zone-face pockets become inequivalent, and the unit cell doubles along the antiferromagnetic direction (which we take here to be X). This doubling produces band folding along the X direction, mapping the electron pockets at X onto the hole pockets at Γ so that a SDW gap appears in locations where the folded bands cross. This folding process leads to a Fermi surface characterized by a central elliptical region from the unhybridized hole pocket and four pockets arising from the SDW Fermi surface reconstruction. The outer pockets along Γ–X are located at q_D. They are protected by orbital symmetry from SDW gap opening and form Dirac cones[45]. This low-temperature Fermi surface is shown in Fig. 4d, modelled from fits to ARPES data[40].

The calculated JDOS created by autocorrelation of the SDW-phase ARPES data is shown in Fig. 4e. This is an excellent match to the STS data at low temperatures, as shown in Fig. 4f, the top half of which is the STS data from Fig. 4a and the bottom half of which is the ARPES JDOS from Fig. 4e. Both the qualitative shape of the STS image and the magnitudes of the scattering wave vectors seen in the STS data are captured by the SDW-phase ARPES JDOS. The origins of the scattering wave vectors seen in the STS data in Fig. 4a are simple to understand on the basis of the ARPES Fermi surface. The four peaks at angles of ∼45° to the Fe–Fe bonds (magenta dotted circle, Fig. 4f) are located at wave vectors that correspond to scattering between the pockets at q_D and the outer pockets along Γ–Y (magenta arrows in Fig. 4d). The intensity enclosed by the yellow dotted line in Fig. 4f along the Γ–Y axis is produced by scattering amongst the pockets aligned along the same axis (yellow arrow in Fig. 4d). The only feature that is not

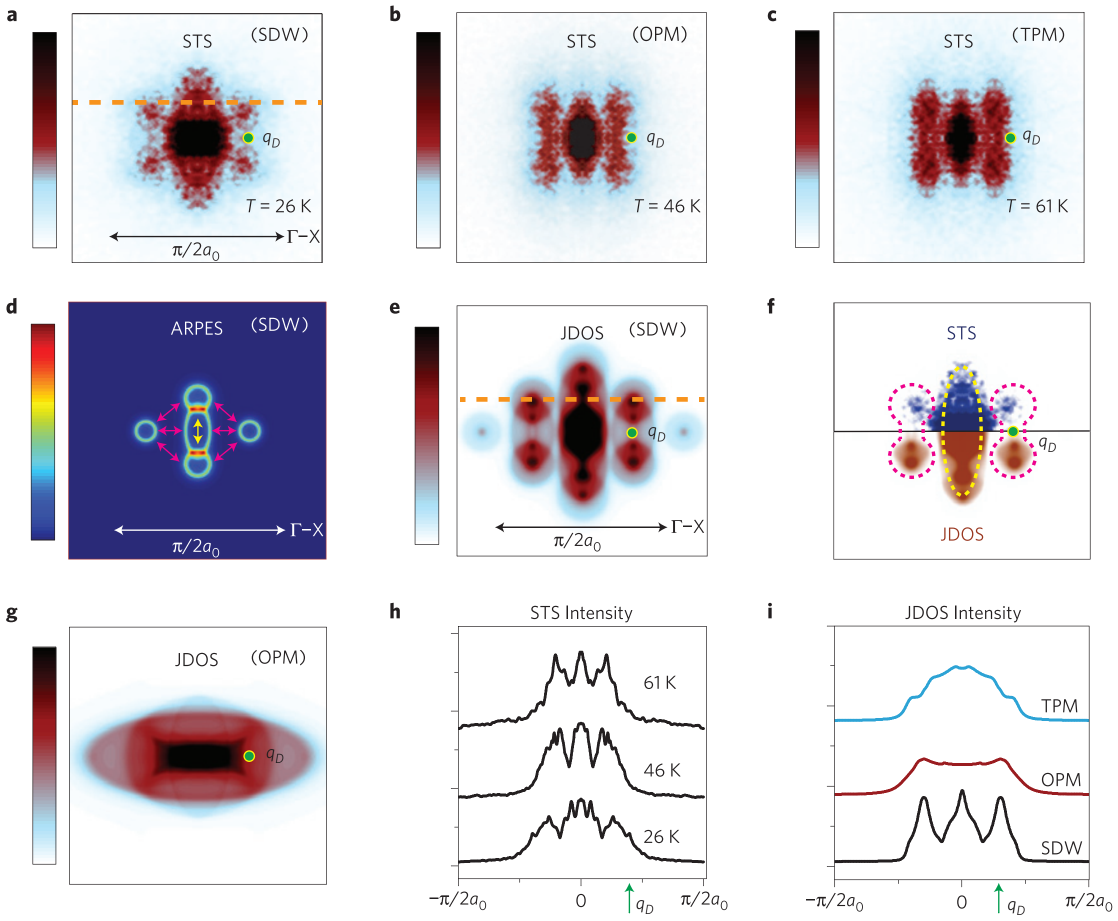

Figure 4 | Comparison between STS and ARPES JDOS. a–c, Fourier transforms of STS images at the Fermi energy for 26, 46 and 61 K respectively. All three STS images show the presence of a strong scattering intensity at $Q_x = 0$ and $Q_x = \pm q_D$ (green dot). **d**, ARPES intensity at the Fermi surface in the SDW ($T < T_{\mathrm{SDW}}$) phase[38]. Magenta arrows indicate scattering that produces 45° peaks in the JDOS, and the yellow arrow corresponds to 0/180° intensity. **e**, JDOS from autocorrelation of SDW ARPES intensity. **f**, SDW STS from **a** placed above the SDW JDOS from **e**. Colour-coded dotted-line contours correspond to scattering peaks that are produced by same coloured scattering vectors as in **d**. **g**, JDOS for OPM phase. The Fermi surface is shown in Supplementary Fig. 5. **h**,**i**, Line cuts of the JDOS and STS along the dotted orange lines in **a** and **e** for different phases/temperatures. Clear peaks arising from reconstructed Fermi surface scattering in the STS data only matches the SDW JDOS.

observed is scattering between the outer pockets at $2q_D$, indicating a suppression of scattering between Dirac cones. The observed STS features are thus well described by the Fermi surface reconstruction due to $(\pi, 0)$ order. We note that, although SDW order is a natural explanation for this reconstruction, other antiferroic orders with the same wave vector (such as antiferro-orbital ordering) can give rise to the same reconstruction of the band structure.

The issue we need to address is why these features persist up to 90 K, above T_{S} and T_{SDW}, where the system is globally tetragonal and paramagnetic. The Fermi surface observed at these temperatures by ARPES is C_4 symmetric, giving rise to a tetragonal symmetric JDOS, at variance with our STS data of Fig. 4c. At intermediate temperatures, between T_{SDW} and T_{S}, SDW order is absent and the band folding does not occur. Yet, as a result of $Q = 0$ ferro-orbital order, the Fermi surface is only C_2 symmetric, as observed by ARPES. In Fig. 4g, we show the JDOS arising from this orthorhombic paramagnetic (OPM) Fermi surface, as determined by ARPES (ref. 40). Although the JDOS still shows C_2 instead of C_4 symmetry, the intensity drops off monotonically away from $Q_x = 0$, unlike what is observed in experiment (Fig. 4b). To illustrate this clearly, we plot in Fig. 4h line cuts through the STS data at $Q_y = 0.1(\pi/a_0)$ (orange dotted line in Fig. 4a), which clearly show three peaks at all temperatures. To compare, we plot in Fig. 4i equivalent line cuts of the joint density of states from ARPES data obtained in the SDW, OPM and tetragonal paramagnetic (TPM) state, respectively. We see that the key feature required to produce the three peaks in the line cuts is the presence of the Fermi surface reconstruction with the wave vector $\mathbf{Q} = ((\pi/a_0), 0)$, which produces disconnected regions of the Fermi surface separated by q_D.

From equation (1), two scenarios may be put forward to explain the data: further structure in the T-matrix, for example due to the impurity nucleating a droplet of ordered phase in its vicinity, or self-energy corrections to the Green's function due to strong local antiferroic (stripe) fluctuations. To gain insight into these two alternatives, we use a simplified band model with two parabolic bands, forming a hole and an electron Fermi pocket. Although this model is too simple to explain all of the details of the experimental data, we will show that it accounts for the crucial qualitative effect, namely the persistence to high temperatures of intensity peaks at $\pm q_D$.

We begin with low temperatures. The reconstructed Fermi surface in the SDW phase is shown in Fig. 5a, and the resulting QPI is shown in Fig. 5b. Comparison of Figs 4d and 5a shows that the key difference between the model and the data is the absence, in the model, of the unhybridized elliptical hole pocket centred at the Gamma point. This pocket produces the central rod structure seen in Fig. 4e, which is absent in Fig. 5b. However, the peaks at ±45° and ±135° arising from the hybridization of the electron and hole pockets are present in the simplified model and in the data.

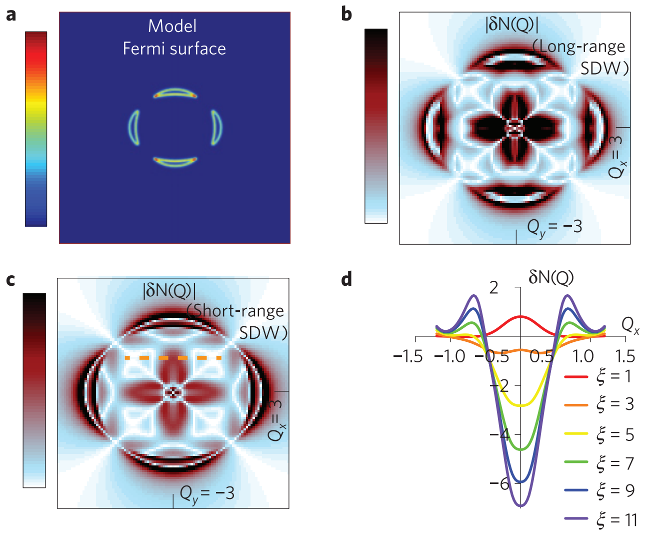

Figure 5 | Theoretical bandstructure and short-range SDW calculations. **a**,**b**, Model Fermi surface density of states (N(**k**)) in **a**, and QPI (|δN(**q**)|) in **b** in the presence of long-range SDW order. **c**, QPI in the presence of short-range ($\xi = 8a_0$) SDW order (see Supplementary Information). **d**, Line cuts along the orange dotted line in **c** for different values of correlation length (in units of a_0). Split peaks develop with increasing correlation length, in analogy to STS data.

We now move to the paramagnetic state. We find (calculation details in Supplementary Information) that calculations based on combining the non-interacting Green's functions of the high-temperature phase (either tetragonal or orthorhombic) with a structured T-matrix corresponding to a local region of SDW order nucleated by the impurity bear no resemblance to the long-range SDW QPI calculation in Fig. 5b. We therefore consider here a model in which the T matrix is structureless but the electron Green's function includes a self-energy correction due to unidirectional, short-range, SDW fluctuations. In this case, we parameterize the short-range correlations by the SDW correlation length ξ and use for the Green's function an ansatz originally introduced in ref. 46 to describe short-range order in charge density wave materials[46]. By increasing ξ to modest values, we find that the calculated QPI spectrum acquires the main features exhibited by the QPI in the SDW phase, even though no SDW long-range order is present. For instance, in Fig. 5c we present the QPI for $\xi = 8a_0$, where we see similar features to those in the calculated QPI of the SDW phase. This becomes more transparent by analysing line cuts along the orange line of Fig. 5c. We see in Fig. 5d that, as ξ increases, the peak at $Q_x = 0$ splits, moving to the same positions as the QPI peaks in the SDW phase. This is in qualitative agreement with the temperature evolution of the experimental QPI cuts shown in Fig. 4i.

Further insight into the nature of the electronic interactions in NaFeAs is obtained by quantifying the C_4 symmetry breaking as a function of energy and temperature. We first crop a small region around each defect in a LDOS image and average all regions together to produce the average spectroscopic image around a single defect. We then rotate the averaged image by 90°, subtract it from the original averaged image, and normalize by the sum of the rotated and unrotated images. This procedure is depicted in Fig. 6a, where we show the unrotated and rotated 26 K defect images at $E = 10$ meV and the resulting 'anisotropy map'. If the original image is C_4 symmetric, then the anisotropy map is zero at every pixel. As such, any non-zero value in the map corresponds to C_4 symmetry breaking. Larger positive or negative values in the anisotropy map correspond to more intense anisotropy. Shown in Fig. 6b–d are three such anisotropy maps from the same temperature as Fig. 6a at three different energies. We can clearly see that the degree of C_4 symmetry breaking decreases with increasing energy. To describe this effect as a function of temperature and energy using a single number (which we call the anisotropy parameter), we sum the absolute value of the intensity in the anisotropy map which we plot in Fig. 6e for several energies at five different temperatures. We note that the anisotropy is strong close to the Fermi energy, peaking slightly above it ($E = 10$ meV), and decreases in strength with increasing temperature. A direct comparison of the energy dependence of the anisotropy parameter with the average spectrum in the SDW state (shown in the inset to Fig. 6e) shows that they share a common energy scale. We take this as another indication that both phenomena share a common origin in the spin physics of the pnictides.

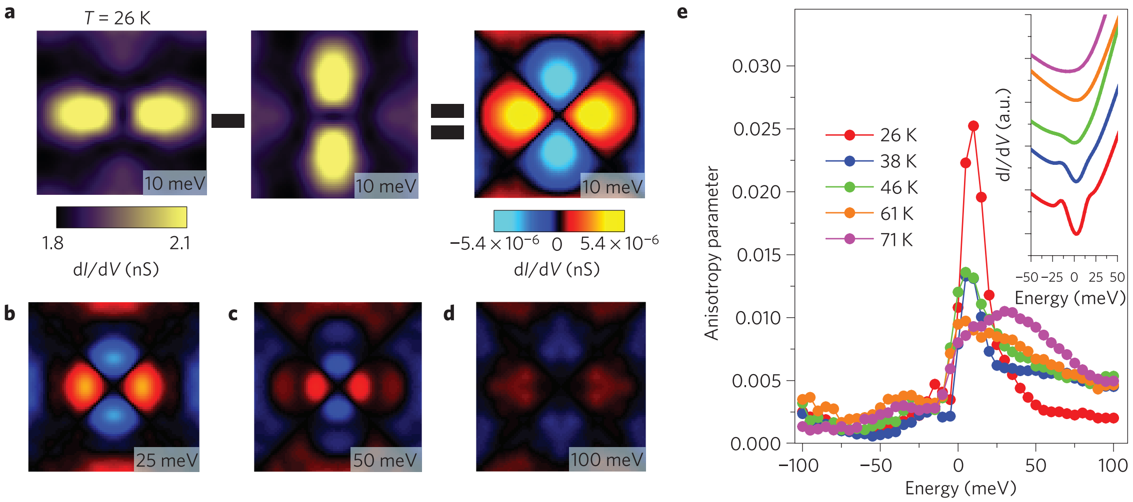

Figure 6 | Energy and temperature dependence of electronic anisotropy. **a**, Visual depiction of the anisotropy map calculation procedure. The average spectroscopic image around a single defect in the SDW phase at $E = 10$ meV and $T = 26$ K is displayed on the left. We rotate the image by 90° (around the centre), subtract it from the original image, and plot the difference (anisotropy map) on the right. **b**–**d**, Anisotropy maps at various energies calculated at the same temperature as **a** and plotted on the same colour scale. The strength of the anisotropy is seen to decrease with increasing energy. **e**, Total anisotropy as a function of energy at various temperatures (junction conditions are the same for all temperatures). It is seen that the anisotropy is maximum at an energy $E = 10$ meV and falls off at higher energy. The average spectrum of the sample at each temperature is shown in the inset. The maximum of the anisotropy is located close to the midpoint of the gap, and the energy range of the anisotropy is comparable to the size of the low-temperature gap.

The breaking of local C_4 symmetry above T_S in the low-energy electronic states, and the association of these features with unidirectional fluctuations (that is, only one of $(0, \pi)$ or $(\pi, 0)$) are the key findings of this experiment. The selection of one fluctuation channel over another is generally believed to be a nonlinear effect signalling that spin fluctuations in one direction have large enough amplitude to suppress fluctuations in the other[21]. Although the antiferroic fluctuations could be due to either orbital (antiferro-orbital) or spin (antiferro-magnetic) degrees of freedom, our finding that the energy dependence of the electronic anisotropy matches the low-temperature SDW gap makes spin fluctuations the natural explanation for the observed anisotropy. Such a redistribution of electronic spectral weight by short-range magnetic order at high temperature is consistent with neutron scattering[47] and nuclear magnetic resonance[48] measurements that observe a clear increase of magnetic fluctuations around the same temperature scale of 90 K in NaFeAs. It is also consistent with the absence of Fermi surface reconstruction in this temperature regime as observed by ARPES, as the zero-energy states are not gapped by short-range SDW order. Interestingly, recent muon spin rotation (μSR) data[49] on another family of iron pnictides found evidence of such short-range SDW order even above the magnetic and structural transitions. The presence of these fluctuations, even far from any phase boundary, must be taken into account in theories of the anomalous pnictide normal state and of the superconductivity arising from it.

Methods

The single crystals of LiFeAs and NaFeAs used for this study were grown by self-flux methods. Li_3As and Na_3As precursors were synthesized by the reaction of Li or Na lumps with As powder at 600 °C for 10 h in an evacuated quartz tube. The FeAs precursor was prepared by sintering the mixture of Fe and As powders at 750 °C for 20 h in an evacuated quartz tube. Later, the Li_3As or Na_3As, FeAs and As powders were mixed according to the stoichiometric ratio of $LiFe_{0.3}As$ or $NaFe_{0.3}As$. The powder mixture was pressed into a pellet in an alumina oxide tube and sealed in a Nb tube with argon gas at a pressure of 1 atm before being sealed in an evacuated quartz tube. This quartz tube was then heated up to a temperature of 1,100 °C for the $LiFe_{0.3}As$ compound or (950 °C for $NaFe_{0.3}As$) for 10 h and then cooled down to 700 °C at a rate of $5\,^\circ\mathrm{C\,h^{-1}}$. We obtained LiFeAs and NaFeAs crystals up to 5 mm × 5 mm × 0.5 mm in size. All the preparation work was carried out inside a glove box protected from air with high-purity Ar gas.

The structural and magnetic transition temperatures of the NaFeAs crystals were characterized with Mossbauer and magnetization measurements. Although these crystals exhibit a superconducting transition around 8 K, the superconducting volume fraction is minimal. We believe the superconductivity to be filamentary and all data presented is measured above the superconducting transition temperature.

STM and STS measurements were carried out using a variable temperature, ultra-high vacuum, home-built STM with millikelvin temperature stability and sub-picometre position accuracy. Single crystal samples were prepared for STM measurements in an Ar glove box by gluing individual crystals to a sample holder using a metallic epoxy. The process of gluing down the crystals has been found to create small but clearly measurable strains in the crystals[12], which we suspect nucleate the large-amplitude, unidirectional fluctuations reported here. We note that in the case of NaFeAs, small strains have little effect on the magnetic and structural transition temperatures themselves[50]. After gluing the samples, they were loaded into the microscope and then cleaved *in situ* between temperatures of 20 and 80 K. Conductance maps were obtained using standard lock-in amplifier techniques with a root mean square oscillation voltage of 1.5 mV and a lock-in frequency of 1.666 kHz. Multiple samples from multiple batches have been measured at various temperatures over a period of several months to rule out tip or sample artefacts, with the tip calibrated on single-crystal gold before each sample measurement.

Received 12 July 2013; accepted 10 December 2013;

References

1. Scalapino, D. J. A common thread: The pairing interaction for unconventional superconductors. *Rev. Mod. Phys.* **84,** 1383–1417 (2012).
2. Wang, F. & Lee, D. H. The electron-pairing mechanism of iron-based superconductors. *Science* **332,** 200–204 (2011).
3. Basov, D. N. & Chubukov, A. V. Manifesto for a higher T_c. *Nature Phys.* **7,** 272–276 (2011).
4. Johnston, D. C. The puzzle of high temperature superconductivity in layered iron pnictides and chalcogenides. *Adv. Phys.* **59,** 803–1061 (2010).
5. Yi, M. *et al.* Symmetry-breaking orbital anisotropy observed for detwinned $Ba(Fe_{1-x}Co_x)_2As_2$ above the spin density wave transition. *Proc. Natl Acad. Sci. USA* **108,** 6878–6883 (2011).
6. De la Cruz, C. *et al.* Magnetic order close to superconductivity in the iron-based layered $LaO_{(1-x)}F_{(x)}FeAs$ systems. *Nature* **453,** 899–902 (2008).
7. Fernandes, R. M. *et al.* Unconventional pairing in the iron arsenide superconductors. *Phys. Rev. B* **81,** 140501(R) (2010).
8. Nandi, S. *et al.* Anomalous suppression of the orthorhombic lattice distortion in superconducting $Ba(Fe_{1-x}Co_x)_2As_2$ single crystals. *Phys. Rev. Lett.* **104,** 057006 (2010).
9. Chu, J. H. *et al.* In-plane resistivity anisotropy in an underdoped iron arsenide superconductor. *Science* **329,** 824–826 (2010).
10. Tanatar, M. A. *et al.* Uniaxial-strain mechanical detwinning of $CaFe_2As_2$ and $BaFe_2As_2$ crystals: Optical and transport study. *Phys. Rev. B* **81,** 184508 (2010).
11. Kasahara, S. *et al.* Electronic nematicity above the structural and superconducting transition in $BaFe_2(As_{1-x}P_x)_2$. *Nature* **486,** 382–385 (2012).
12. Chu, J. H., Kuo, H. H., Analytis, J. G. & Fisher, I. R. Divergent nematic susceptibility in an iron arsenide superconductor. *Science* **337,** 710–712 (2012).
13. Gallais, Y. *et al.* Observation of incipient charge nematicity in $Ba(Fe_{1-x}Co_x)_2As_2$. *Phys. Rev. Lett.* **111,** 267001 (2013).
14. Dusza, A. *et al.* Anisotropic charge dynamics in detwinned $Ba(Fe_{1-x}Co_x)_2As_2$. *Europhys. Lett.* **93,** 37002 (2011).
15. Nakajima, M. *et al.* Unprecedented anisotropic metallic state in undoped iron arsenide $BaFe_2As_2$ revealed by optical spectroscopy. *Proc. Natl Acad. Sci. USA* **108,** 12238–12242 (2011).
16. Dhital, C. *et al.* Effect of uniaxial strain on the structural and magnetic phase transitions in $BaFe_2As_2$. *Phys. Rev. Lett.* **108,** 087001 (2012).
17. Fang, C., Yao, H., Tsai, W. F., Hu, J. P. & Kivelson, S. A. Theory of electron nematic order in LaFeAsO. *Phys. Rev. B* **77,** 224509 (2008).
18. Xu, C., Muller, M. & Sachdev, S. Ising and spin orders in the iron-based superconductors. *Phys. Rev. B* **78,** 020501(R) (2008).
19. Mazin, I. I. & Johannes, M. D. A key role for unusual spin dynamics in ferropnictides. *Nature Phys.* **5,** 141–145 (2009).
20. Fernandes, R. M., Abrahams, E. & Schmalian, J. Anisotropic in-plane resistivity in the nematic phase of the iron pnictides. *Phys. Rev. Lett.* **107,** 217002 (2011).
21. Fernandes, R. M., Chubukov, A. V., Knolle, J., Eremin, I. & Schmalian, J. Preemptive nematic order, pseudogap, and orbital order in the iron pnictides. *Phys. Rev. B* **85,** 024534 (2012).
22. Lv, W. C. & Phillips, P. Orbitally and magnetically induced anisotropy in iron-based superconductors. *Phys. Rev. B* **84,** 174512 (2011).
23. Chen, C. C. *et al.* Orbital order and spontaneous orthorhombicity in iron pnictides. *Phys. Rev. B* **82,** 100504(R) (2010).
24. Kontani, H., Saito, T. & Onari, S. Origin of orthorhombic transition, magnetic transition, and shear-modulus softening in iron pnictide superconductors: Analysis based on the orbital fluctuations theory. *Phys. Rev. B* **84,** 024528 (2011).
25. Song, C. L. *et al.* Direct observation of nodes and twofold symmetry in FeSe superconductor. *Science* **332,** 1410–1413 (2011).
26. Chuang, T. M. *et al.* Nematic electronic structure in the 'Parent' state of the iron-based superconductor $Ca(Fe_{1-x}Co_x)_2As_2$. *Science* **327,** 181–184 (2010).
27. Zhou, X. D. *et al.* Quasiparticle interference of C_2-symmetric surface states in a LaOFeAs parent compound. *Phys. Rev. Lett.* **106,** 087001 (2011).
28. Zhou, X. D. *et al.* Evolution from unconventional spin density wave to superconductivity and a pseudogaplike phase in $NaFe_{1-x}Co_xAs$. *Phys. Rev. Lett.* **109,** 037002 (2012).
29. Hanke, T. *et al.* Probing the unconventional superconducting state of LiFeAs by quasiparticle interference. *Phys. Rev. Lett.* **108,** 127001 (2012).
30. Allan, M. P. *et al.* Anisotropic energy gaps of iron-based superconductivity from intraband quasiparticle interference in LiFeAs. *Science* **336,** 563–567 (2012).
31. Hanaguri, T. *et al.* Scanning tunneling microscopy/spectroscopy of vortices in LiFeAs. *Phys. Rev. B* **85,** 214505 (2012).
32. Grothe, S. *et al.* Bound states of defects in superconducting LiFeAs studied by scanning tunneling spectroscopy. *Phys. Rev. B.* **86,** 174503 (2012).
33. Wang, X. C. *et al.* The superconductivity at 18 K in LiFeAs system. *Solid State Commun.* **148,** 538–540 (2008).
34. Tapp, J. H. *et al.* LiFeAs: An intrinsic FeAs-based superconductor with $T_c = 18\,\mathrm{K}$. *Phys. Rev. B* **78,** 060505(R) (2008).
35. Chu, C. W. *et al.* The synthesis and characterization of LiFeAs and NaFeAs. *Physica C* **469,** 326–331 (2009).
36. Kalisky, B. *et al.* Stripes of increased diamagnetic susceptibility in underdoped superconducting $Ba(Fe_{(1-x)}Co_x)_2As_2$ single crystals: Evidence for an enhanced superfluid density at twin boundaries. *Phys. Rev. B* **81,** 184513 (2010).

37. Allan, M. P. *et al.* Anisotropic impurity states, quasiparticle scattering and nematic transport in underdoped $Ca(Fe_{1-x}Co_x)_2As_2$. *Nature Phys.* **9,** 220–224 (2013).
38. Knolle, J., Eremin, I., Akbari, A. & Moessner, R. Quasiparticle interference in the spin-density wave phase of iron-based superconductors. *Phys. Rev. Lett.* **104,** 257001 (2010).
39. Crommie, M. F., Lutz, C. P. & Eigler, D. M. Imaging standing waves in a two-dimensional electron gas. *Nature* **363,** 524–527 (1993).
40. Yi, M. *et al.* Electronic reconstruction through the structural and magnetic transitions in detwinned NaFeAs. *New J. Phys.* **14,** 073019 (2012).
41. Zhang, Y. *et al.* Symmetry breaking via orbital-dependent reconstruction of electronic structure in detwinned NaFeAs. *Phys. Rev. B* **85,** 085121 (2012).
42. Wang, A. F. *et al.* A crossover in the phase diagram of $NaFe_{1-x}Co_xAs$ determined by electronic transport measurements. *New J. Phys.* **15,** 043048 (2013).
43. Wang, Q. H. & Lee, D. H. Quasiparticle scattering interference in high-temperature superconductors. *Phys. Rev. B* **67,** 020511(R) (2003).
44. Chatterjee, U. *et al.* Nondispersive fermi arcs and the absence of charge ordering in the pseudogap phase of $Bi_2Sr_2CaCu_2O_{8+\delta}$. *Phys. Rev. Lett.* **96,** 107006 (2006).
45. Ran, Y., Wang, F., Zhai, H., Vishwanath, A. & Lee, D. H. Nodal spin density wave and band topology of the FeAs-based materials. *Phys. Rev. B* **79,** 014505 (2009).
46. Lee, P. A., Rice, T. M. & Anderson, P. W. Fluctuation effects at a Peierls transition. *Phys. Rev. Lett.* **31,** 462–465 (1973).
47. Park, J. T. *et al.* Similar zone-center gaps in the low-energy spin-wave spectra of $Na_{1-\delta}$ FeAs and $BaFe_2As_2$. *Phys. Rev. B* **86,** 024437 (2012).
48. Ma, L. *et al.* Na-23 and As-75 NMR study of antiferromagnetism and spin fluctuations in NaFeAs single crystals. *Phys. Rev. B* **83,** 132501 (2011).
49. Maeter, H. *et al.* Structural and electronic phase diagrams of $CeFeAsO_{1-x}F_x$ and $SmFeAsO_{1-x}F_x$. Preprint at http://arxiv.org/abs/1210.6959 (2012).
50. Song, Y. *et al.* Uniaxial pressure effect on structural and magnetic phase transitions in NaFeAs and its comparison with as-grown and annealed $BaFe_2As_2$. *Phys. Rev. B* **87,** 184511 (2013).

Acknowledgements

We thank L. Zhao and C. Gutierrez for experimental help and T. Giamarchi and I. Eremin for discussions. We thank M. Yi and Z-X. Shen for sharing ARPES data on NaFeAs. This work is supported by the National Science Foundation through the Partnerships for International Research and Education grant no. OISE-0968226 and Defense Advanced Research Projects Agency grant no. N66001-12-1-4216 (A.N.P. and E.P.R.). Equipment support is provided by the Air Force Office for Scientific Research under grant no. FA9550-11-1-0010. Support is also provided by the National Science Foundation through grant no. NSF-DMR 1006282 (A.J.M.) and the National Science Foundation of China and Ministry of Science and Technology of China (L.Y.X., X.C.W. and C.Q.J.).

Author contributions

STM experiments and data analysis: E.P.R., E.F.A., C.J.A. and A.N.P. Theoretical analysis: R.M.F. and A.J.M. Sample synthesis and characterization: L.Y.X., X.C.W. and C.Q.J. All authors participated in writing the manuscript.

Additional information

Supplementary information is available in the online version of the paper. Reprints and permissions information is available online at www.nature.com/reprints. Correspondence and requests for materials should be addressed to A.N.P.

Competing financial interests

The authors declare no competing financial interests.